

Forming Gliese 876 Through Smooth Disk Migration

ADAM M. DEMPSEY¹ AND BENJAMIN E. NELSON^{1,2}

¹*Center for Interdisciplinary Exploration and Research in Astrophysics (CIERA) and Department of Physics and Astronomy
Northwestern University*

2145 Sheridan Road Evanston, IL 60208 USA

²*Northwestern Institute for Complex Systems
600 Foster Street Evanston, IL 60208 USA*

ABSTRACT

We run a suite of dissipative N-body simulations to determine which regions of phase space for smooth disk migration are consistent with the GJ876 system, an M-dwarf hosting three planets orbiting in a chaotic 4:2:1 Laplace resonance. We adopt adaptive mesh refinement (AMR) methods which are commonly used in hydrodynamical simulations to efficiently explore the parameter space defined by the semi-major axis and eccentricity damping timescales. We find that there is a large region of phase space which produces systems in the chaotic Laplace resonance and a smaller region consistent with the observed eccentricities and libration amplitudes for the resonant angles. Under the assumptions of Type I migration for the outer planet, we translate these damping timescales into constraints on the protoplanetary disk surface density and thickness. When we strongly (weakly) damp the eccentricities of the inner two Laplace planets, these timescales correspond to disk surface densities around ten thousand (a few hundred) grams per square centimeter and disk aspect ratios between 1 – 10%. Additionally, smooth migration produces systems with a range of chaotic timescales, from decades and centuries to upwards of thousands of years. In agreement with previous studies, the less chaotic regions of phase space coincide with the system being in a low energy double apsidal corotation resonance. Our detailed modeling of multi-planetary systems coupled with our AMR exploration method enhances our ability to map out the parameter space of planet formation models, and is well suited to study other resonant chain systems such as Trappist-1, Kepler-60, and others.

Keywords: celestial mechanics — planet-disk interactions — planets and satellites: dynamical evolution and stability

1. INTRODUCTION

Gliese 876 (GJ876) is an M-dwarf star ($M_{\star} \simeq 0.37M_{\odot}$) 4.6 pc away that harbors a well-studied multi-planetary system (Marcy et al. 1998; van Leeuwen 2007; von Braun et al. 2014). Through radial velocity measurements, we know of at least four planets orbiting GJ876, the outer three of which are in a 4:2:1 (Laplace) mean-motion resonance (MMR) (Rivera et al. 2010). Leveraging the strong resonant interactions, several studies have been able to break the mass and inclination degeneracy of the system, providing strong constraints on the full orbital parameters and planetary masses (Correia et al. 2010; Rivera et al. 2010; Nelson et al. 2016; Trifonov et al. 2018; Millholland et al. 2018). Of partic-

ular note is that the system is chaotic on potentially observable timescales, and that the mass ratios of GJ876-c ($M_c \simeq 265M_{\oplus}$, $P_c = 30d$, $e_c = 0.26$) and GJ876-b ($M_b \simeq 845M_{\oplus}$, $P_b = 61d$, $e_b = 0.036$) are large enough to potentially open a deep and wide gap in their natal disk – possibly extending out to the outermost planet, GJ876-e ($M_e \simeq 16M_{\oplus}$, $P_e = 124d$, $e_e \simeq 0.03$) (Snellgrove et al. 2001; Rein et al. 2010).

Recently, Batygin et al. (2015) investigated the formation of GJ876 through *stochastic* disk migration. They attributed the stochasticity to turbulence in the disk, and argued that it was essential for producing the observed chaotic state of the system. Historically, the magnetorotational instability (MRI) was thought to be the driver of turbulence in protoplanetary disks (Balbus & Hawley 1991). However, recent simulations have shown that non-ideal MHD processes can suppress or

completely shutoff the MRI in the midplanes of protoplanetary disks where planets are expected to form (e.g. Bai & Stone 2013; Lesur et al. 2014; Simon et al. 2015). If these regions are laminar or weakly turbulent, then stochastic forcing of a smoothly migrating planet may be negligible. It then becomes important to know whether or not smooth migration alone can account for all of the observed characteristics of GJ876. Moreover, while previous studies have focused on constructing the 2:1 resonance of GJ876-c,b through smooth migration (e.g., Lee & Peale 2002), there has yet to be an exhaustive analysis focused on constructing the chaotic Laplace resonance through disk migration.

This paper is organized as follows. In §2 we outline our procedure for simulating the migration history of GJ876 and our method for efficiently exploring parameter space. In §3 we present the main results from our suite of simulations. In §4 we explore several different variations on the procedure outlined in §2. Finally, we end in §5 by discussing improvements to our smooth migration model and the possibility of extending our procedure to other resonant chain exoplanet systems.

2. NUMERICAL MODEL

2.1. Smooth migration

Smooth migration models attempt to parameterize the complex energy and angular momentum transfer processes between a planet and its surrounding disk by specifying the exponential damping timescales associated with semi-major axis evolution, $\tau_a \equiv |a/\dot{a}|$, and eccentricity evolution, $\tau_e \equiv |e/\dot{e}|$ (for a review see e.g. Kley & Nelson 2012). The damping timescales for a planet of mass M_p orbiting a star of mass M_\star at semi-major axis a and orbital period P are,

$$\tau_a^{-1} = C_a \left(\frac{4\pi a^2 \Sigma_p M_p}{M_\star^2} \right) \left(\frac{H}{a} \right)^{-2} P^{-1}, \quad (1)$$

$$\tau_e^{-1} = C_e \left(\frac{4\pi a^2 \Sigma_p M_p}{M_\star^2} \right) \left(\frac{H}{a} \right)^{-4} P^{-1}, \quad (2)$$

where Σ_p and H/a are the surface density and aspect ratio of the disk at the location of the migrating planet (Goldreich & Tremaine 1980). We adopt the proportionality constants $C_a = 2.175$ and $C_e = 0.39$ (Tanaka et al. 2002; Tanaka & Ward 2004), but note that they depend strongly on the local disk structure (e.g. Goldreich & Tremaine 1980, 1981; Artymowicz 1993a,b; Goldreich & Sari 2003; Kley & Nelson 2012). Equations (1) and (2) correspond to the so-called Type I migration regime (Ward 1997; Goldreich & Schlichting 2014). The ratio of these timescales, K , depends on the local disk aspect

ratio as,

$$K \equiv \frac{\tau_a}{\tau_e} \propto \left(\frac{H}{a} \right)^{-2}. \quad (3)$$

In the N-body simulations presented in the next section, we only apply semi-major axis damping forces to GJ876-e as its migration rate should be relatively fast compared to the slow Type II migration rates of GJ876-c,b (e.g. Kley & Nelson 2012; Dürmann & Kley 2015). However, since the eccentricity damping rates of the inner planets may be faster than their semi-major axis damping rates by a factor of K , and given that the equilibrium eccentricities of planets migrating in MMR depend on their eccentricity damping timescale (e.g. Lee & Peale 2002; Goldreich & Schlichting 2014), we apply eccentricity damping forces to the planets GJ876-c,b with a damping timescale denoted by $\tau_{e,1}$, in our N-body simulations.

2.2. Simulation setup

Our goal is to map out the parameter space in K , τ_a , and $\tau_{e,1}$ for the system properties of GJ876. Our simulation procedure is similar to that of Tamayo et al. (2017), who studied the formation history of the Trappist-1 resonant chain. For a given K , τ_a , and $\tau_{e,1}$ we first initialize a coplanar, three planet system around a $M_\star = 1M_\odot$ star. The masses of the three planets are chosen to reproduce the best fit mass ratios of planets GJ876-c,b and e (which we henceforth label as planets 1, 2, and 3). These are set to $M_1 = 2.15 \times 10^{-3}M_\star$, $M_2 = 6.85 \times 10^{-3}M_\star$, and $M_3 = 1.30 \times 10^{-4}M_\star$ (Millholland et al. 2018). The initial orbital periods are $P_1 = 1$ year, $P_2/P_1 = 2.2$, and $P_3/P_2 = 10$. Once initialized, we integrate each planetary system for a time of $10\tau_a$ while applying the aforementioned damping forces.

After this initial damping phase, we remove all damping forces from the system over a time of τ_a . If the system is in the Laplace resonance, we rescale the system to the observed properties of GJ876. This entails changing the mass of the central star to $M_\star = 0.37M_\odot$ and the inner planet's period to the observed period of GJ876-c, all while keeping the planet-to-star mass ratios and period ratios the same as in the previous phase. Finally, we integrate the rescaled system without any damping forces for 10^5 years. This rescaling of the simulation after the migration phase is similar to what was done in Tamayo et al. (2017) for the Trappist-1 system, and allows us to avoid having to fine tune the initial conditions or adjust the duration of the damping phase so that the planets end up near their observed periods by the end of the damping period.

All integrations are done with the REBOUND¹ N-body code (Rein & Liu 2012). For the damping forces we use the REBOUND extension REBOUNDX² to introduce orbit-averaged forces which give the proper damping timescales (Papaloizou & Larwood 2000). We use the WHFast integrator for all simulations with 40 timesteps per initial orbital period of the inner planet (Rein & Tamayo 2015). We found this to be in good agreement with simulations run with the more accurate (but slower) IAS15 integrator (Rein & Spiegel 2015).

We show the time evolution of the planetary periods, eccentricities, Laplace resonance angle, and two 2:1 resonance angles of a representative simulation in Figure 1. The Laplace angle is defined in terms of the mean longitudes, λ , of the planets as $\Phi_L = \lambda_1 - 3\lambda_2 + 2\lambda_3$. The 2:1 MMR resonant angles are defined as $\Phi_{1,2} = 2\lambda_2 - \lambda_1 - \varpi_2$ and $\Phi_{2,3} = 2\lambda_3 - \lambda_2 - \varpi_2$, where ϖ denotes the longitude of pericenter. In this example simulation, for times less than $10\tau_a$ the outer planet experiences damping forces with $\log_{10} K = 3.125$ and $\tau_a = 10^4 P_1$. The inner planets also experience eccentricity damping forces with $\tau_{e,1} = 10^{5.5} P_1$. During this phase the planets are brought into successive 2:1 MMRs, evidenced by $\Phi_{1,2}$ and $\Phi_{2,3}$ librating about 0° with small amplitude. At nearly the same time the system also catches into the Laplace resonance. As the system continues to migrate while in the 4:2:1 resonance, the eccentricity of the inner planet grows to $e_1 \approx 0.25$, while $e_2 \approx e_3 \approx 0.03$. Between times of $10\tau_a$ and $11\tau_a$, which corresponds to the region between the two vertical dashed lines in Figure 1, we gradually remove the damping forces. Then at a time of $11\tau_a$ we completely remove all damping forces and rescale the system to an inner period of 30 days and a central mass of $0.37M_\odot$. Finally, we evolve the system for 10^5 years where it remains in a stable, resonant configuration.

2.3. Efficiently exploring parameter space

To efficiently sample the 3D parameter space of K , τ_a , and $\tau_{e,1}$, we adopt the techniques of adaptive mesh refinement (AMR; Berger & Colella 1989) to focus most of our computational efforts on parts of parameter space where the system is in the Laplace resonance. The "mesh" used here is the discretized 3D parameter space of $(K, \tau_a, \tau_{e,1})$, where at each point on the mesh we run an N-body simulation. We apply the refinement procedure of Löhner (1987) (see also e.g. Fryxell et al. 2000) to the RMS libration amplitude of the Laplace angle.

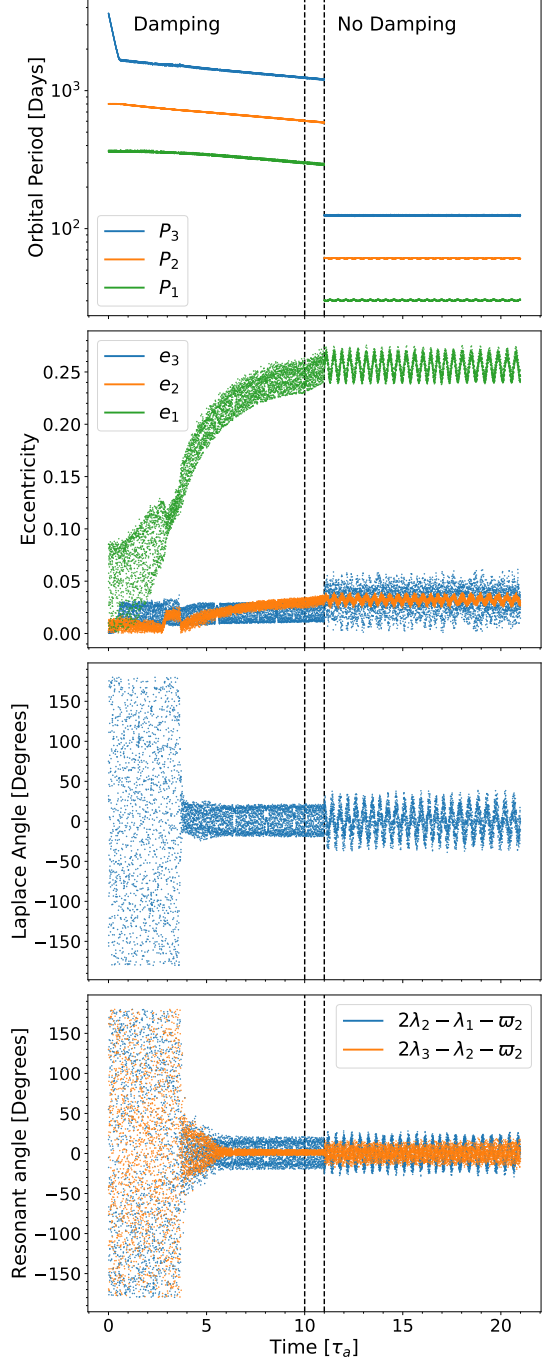


Figure 1. Time evolution of a simulation with $(\log_{10}(K), \log_{10}(\tau_a/P_1), \log_{10}(\tau_{e,1}/P_1)) = (3.125, 4, 5.5)$ demonstrating our simulation procedure. The vertical lines mark the end of the initial damping phase and the start of the damping-free phase. During this time period the damping forces on the planets are reduced to zero over a time of τ_a . At the beginning of the damping-free phase we rescale the system to the observed period of the inner planet. In descending order, the panels show the time evolution of the orbital periods, eccentricities, the Laplace resonant angle, and two, 2:1 MMR angles.

¹ <http://github.com/hannorein/rebound>, v3.5.2.

² <http://github.com/dtamayo/reboundx>, v2.18.1.

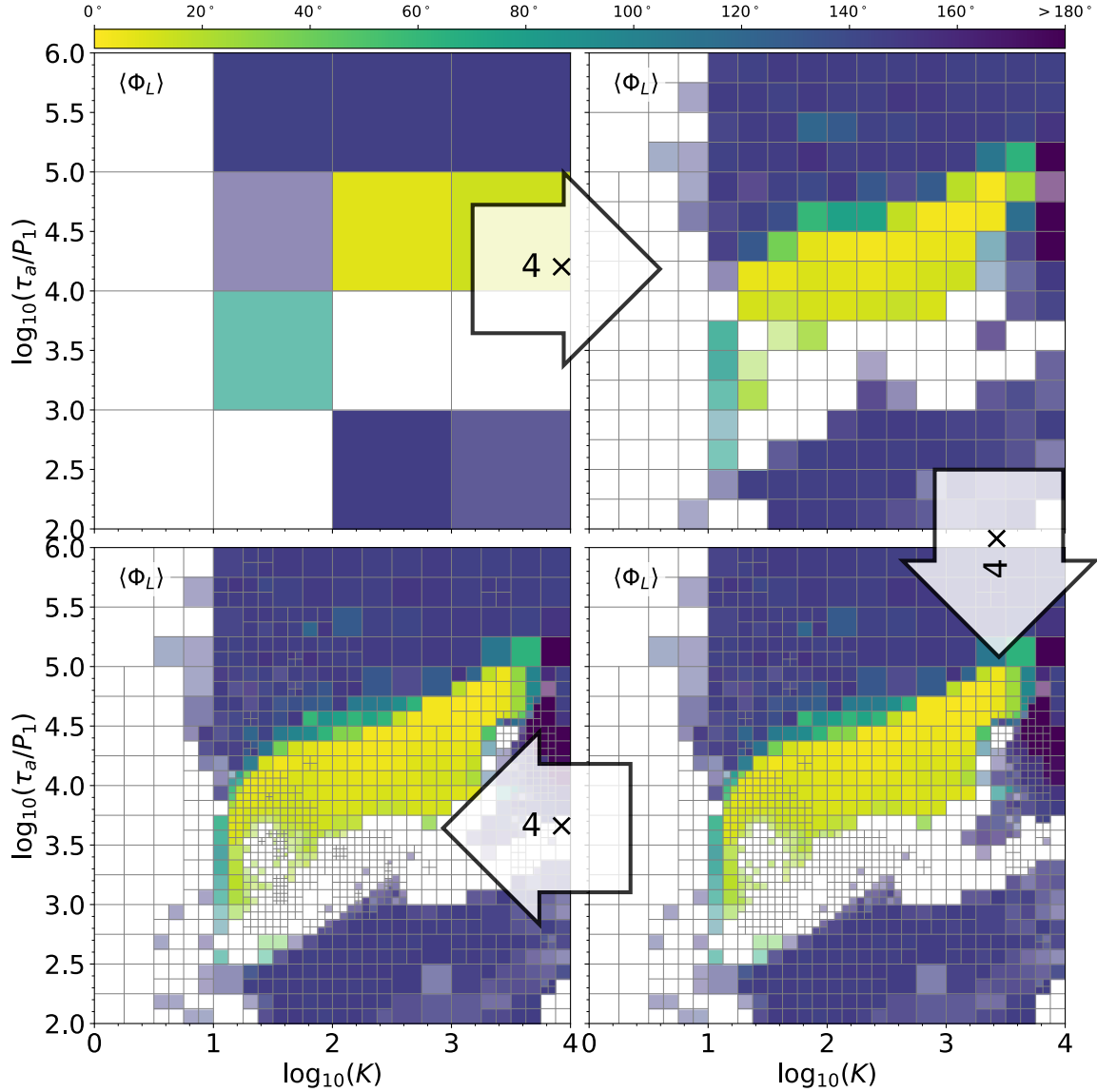


Figure 2. The Laplace angle libration amplitude and our AMR grid in τ_a and $K = \tau_a/\tau_e$ space for fixed $\tau_{e,1} = 10^5 P_1$, at increasing levels of refinement. The color of each cell is the average libration amplitude of 10 simulations where the initial angles were randomized. The opacity of each cell indicates its instability fraction, with white cells indicating that all 10 simulations went unstable. The observed libration amplitude of GJ876 is approximately $26^\circ \pm 5^\circ$ (Millholland et al. 2018).

We define the RMS libration amplitude as,

$$\langle \Phi_L \rangle = \sqrt{\frac{2}{T} \int_{t_{\text{final}}-T}^{t_{\text{final}}} dt \Phi_L^2(t)}, \quad (4)$$

where the averaging time $T = 10^4 P_1$ for resonant systems³. We focus our refinement on regions where $\langle \Phi_L \rangle < 100^\circ$ and where there is a boundary between

³ For simulations that do not catch into resonance the averaging time is 10% of τ_a .

an unstable⁴ cell and a cell in resonance. Our adaptive grid uses up to 8 refinement levels, with each refinement level doubling the number of points in K , τ_a , and $\tau_{e,1}$, respectively. Our final grid has an effective uniform resolution of 256^3 logarithmically spaced points in the domain $\tau_a \in [10^2, 10^6] P_1$, $K \in [1, 10^4]$, and $\tau_{e,1} \in [10^4, 10^8] P_1$ ⁵. We determine the AMR grid through one set of simu-

⁴ For simplicity we define "unstable" to mean an ejection of a planet from the system or when the Hill spheres of two planets overlap.

⁵ Preliminary simulations ruled out regions where $\tau_a < 10^2 P_1$, $K > 10^4$, and $\tau_{e,1} < 10^4 P_1$.

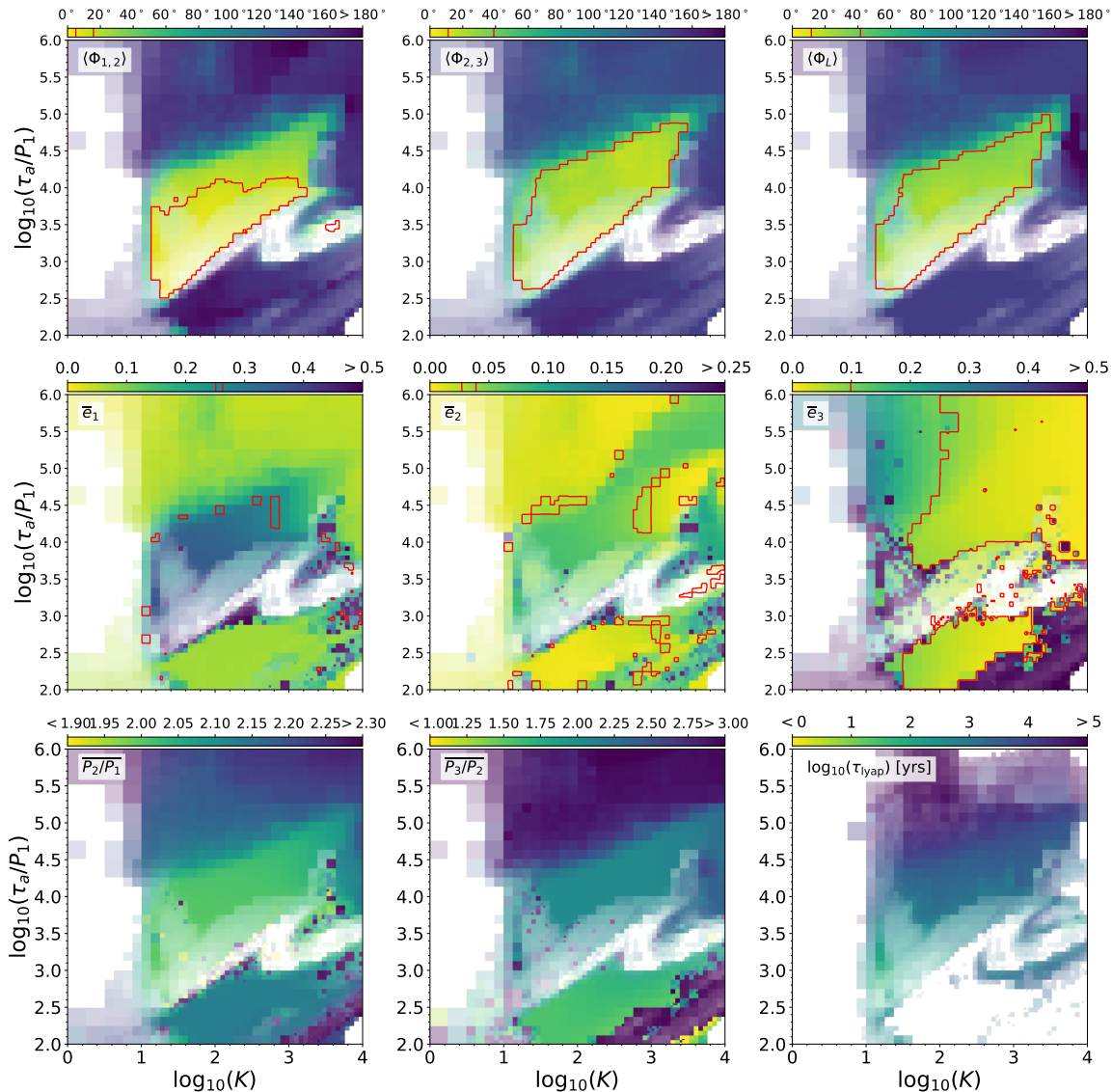


Figure 3. Overview of the resonant angles (top row), eccentricities (middle row), inner and outer period ratios, and Lyapunov time (bottom row) for the simulation procedure described in §2.2. All quantities are averaged over $\tau_{e,1}$. An overbar denotes the time-averaged value, while angle brackets denote the RMS libration amplitude. When present, regions falling within the red contours signify $\leq 3\sigma$ agreement with the observed values from Millholland et al. (2018) (see §3.3). In the Lyapunov time plot, simulations which did not catch into the Laplace resonance by the end of the damping phase are not shown (see §3.4).

lations, and then repeat each simulation with randomized initial phase angles for a total of 10 simulations per $(K, \tau_a, \tau_{e,1})$.

In Figure 2 we show our AMR grid and $\langle \Phi_L \rangle$ for a slice at $\tau_{e,1} = 10^5 P_1$. The opacity of each cell shows the instability fraction, with white cells indicating that all 10 initial conditions for that $(K, \tau_a, \tau_{e,1})$ point went unstable. In the end, we run a total of ~ 1.3 million simulations, roughly two orders of magnitude less than the ~ 160 million simulations required to have a uniform resolution of 256^3 points over our range of K , τ_a , and $\tau_{e,1}$. These savings allow us to explore several different

variations on the setup described in §2.2, which we detail further in §4.1.

3. RESULTS

Our main results are shown in Figure 3, where we plot the (K, τ_a) distributions, integrated over $\tau_{e,1}$, of several important quantities, and in Figures 4–6, where we show the $\tau_{e,1}$ dependence of Φ_L and e_1 at several slices of constant τ_a and K .

3.1. Resonant angles and period ratios

The top row of Figure 3 shows the libration amplitudes of the two-body, 2:1 resonance angles, $\Phi_{1,2} =$

$2\lambda_2 - \lambda_1 - \varpi_2$, $\Phi_{2,3} = 2\lambda_3 - \lambda_2 - \varpi_2$, and Φ_L . We find that the majority of parameter space does not produce systems in the Laplace resonance. Rather, there is a bounded resonant region where the libration amplitudes of $\Phi_{1,2}$, $\Phi_{2,3}$, and Φ_L tend to be smallest in the center and quickly rise (or become unstable) at the edges. We argue in the next section that the instabilities at $K \lesssim 10$ are the result of the eccentricity of the outer planet increasing to the point of orbit-crossing with the middle planet, while the instabilities at $K \gtrsim 10$ are primarily due to high eccentricities of the inner planet. The observed libration amplitude of Φ_L is of moderate to large amplitude ($\simeq 20^\circ - 30^\circ$; Nelson et al. 2016; Millholland et al. 2018), and so we are primarily interested in the transitional regions of parameter space.

The bottom row of Figure 3 shows the period ratios for the inner and outer pair of planets. Since we start the outer planet well outside the 3:1 MMR, the outer two planets catch into MMRs with period ratios greater than 2 for slow enough damping timescales. This is not the case for the inner pair of planets, as they are initially placed just wide of the 2:1 resonance. Moreover, once the outer pair is locked into resonance, the effective migration rate slows by a factor dependent on the mass ratios (Lee & Peale 2002). This reduction of the effective migration rate makes it easier for the inner pair of planets to capture into the 2:1 resonance, rather than push through to the 3:2 MMR (Goldreich & Schlichting 2014).

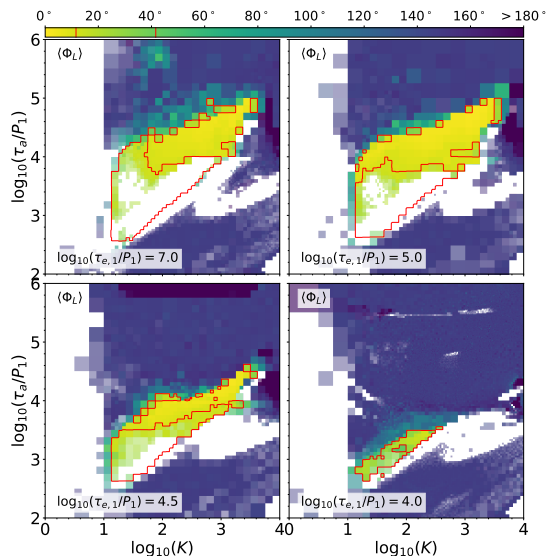


Figure 4. Similar to Figure 3, but we focus on the Laplace angle libration amplitude for four constant values of $\tau_{e,1}$: 10^4 , $10^{4.5}$, 10^5 and $10^7 P_1$. As $\tau_{e,1}$ decreases, the resonant region shrinks and moves to lower τ_a and K .

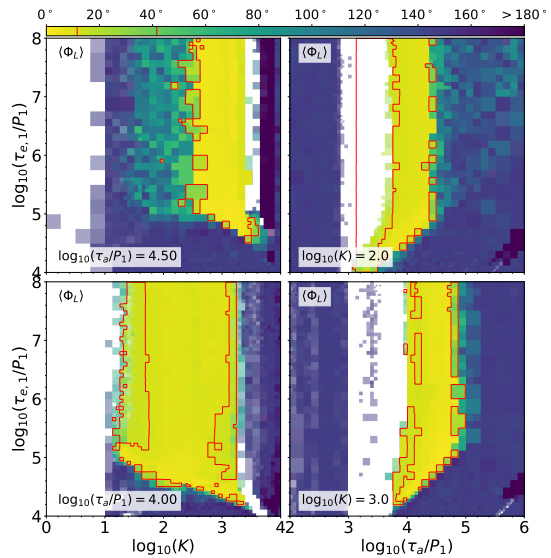


Figure 5. Similar to Figure 4, but for slices through parameter space for constant τ_a (left column) and constant K (right column) for the Laplace angle libration amplitude. The τ_a slices are $10^4 P_1$ and $10^{4.5} P_1$, while the K slices are at 10^2 and 10^3 .

In Figure 4 we show the libration amplitude of Φ_L for four different values of $\tau_{e,1}$: $10^4 P_1$, $10^{4.5} P_1$, $10^5 P_1$, and $10^7 P_1$. As $\tau_{e,1}$ decreases the stable Laplace resonance region shrinks and shifts towards lower τ_a and lower K which were unstable at larger values of $\tau_{e,1}$. The magnitude of $\langle \Phi_L \rangle$ is also typically larger for lower $\tau_{e,1}$. Note that the unstable region for $K \lesssim 10$ is relatively robust to the value of $\tau_{e,1}$, reinforcing the understanding that this is connected to the large eccentricity of the outer planet. On the other hand, the region of instability at the lower end of the resonant region for $K \gtrsim 10$ shrinks as $\tau_{e,1}$ decreases, as the equilibrium eccentricity of the inner planet is lower (see also Figure 6).

Similar to Figure 4, Figure 5 shows $\langle \Phi_L \rangle$ for cuts of constant τ_a and K . In the left panels, we show the $(K, \tau_{e,1})$ dependence of $\langle \Phi_L \rangle$ for $\tau_a = 10^4 P_1$ and $10^{4.5} P_1$, while in the right panels we show the $(\tau_a, \tau_{e,1})$ dependence for $K = 10^2$ and 10^3 . In all cases, $\langle \Phi_L \rangle$ is roughly independent of $\tau_{e,1}$ until $\tau_{e,1} \sim \tau_a$ at which point the system quickly escapes from the Laplace resonance.

3.2. Eccentricities

The middle row of Figure 3 shows the final time-averaged eccentricities of each simulation. When in the three-body resonance, the inner planet's eccentricity is typically pumped to large values ($e_1 \sim 0.4$ for large $\tau_{e,1}$), while e_2 remains low, and e_3 increases as K decreases. Figure 6 shows the $\tau_{e,1}$ dependence of e_1 for the same constant values of τ_a and K as discussed previously in Figure 5. Similar to $\langle \Phi_L \rangle$, for fixed τ_a and K , the in-

ner planet’s eccentricity is roughly independent of $\tau_{e,1}$ when $\tau_{e,1}$ is large. When $\tau_{e,1}$ becomes comparable in magnitude to τ_a the inner planet reaches an equilibrium eccentricity lower than $e_1 \sim 0.4$. However, the transition to $e_1 < 0.2$ is relatively quick as $\tau_{e,1}$ decreases while the transition is more gradual for fixed $\tau_{e,1}$ and increasing either τ_a or K .

In the next section, we explore more quantitatively how well our simulated systems compare to the observed GJ876.

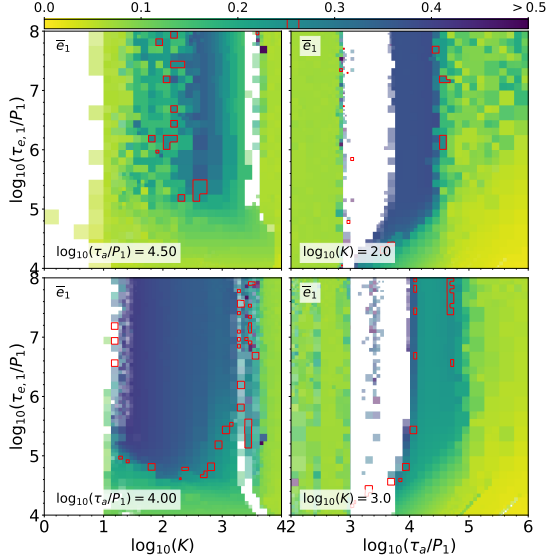


Figure 6. Same as Figure 5, but for the eccentricity of the inner planet.

3.3. Comparison to the real GJ876

The red contours in Figures 3-6 show the 3σ contours of the observed values for the three resonant angles, $\Phi_{1,2} = 10.4^\circ \pm 1.8^\circ$, $\Phi_{2,3} = 25.0^\circ \pm 4.65^\circ$, $\Phi_L = 26.6^\circ \pm 5.0^\circ$, and three eccentricities, $e_1 = 0.257 \pm 0.002$, $e_2 = 0.033 \pm 0.002$, and $e_3 = 0.03 \pm 0.023$, taken from Millholland et al. (2018). For simplicity, we have averaged any asymmetric errors.

The resonant angles are within the 3σ contours for a wide range of K , τ_a , and $\tau_{e,1}$. The eccentricities of the inner planets, on the other hand, are near their observed values in a much narrower range of parameter space. This suggests that the inner planets’ eccentricities provide a strong constraint on the region of parameter space consistent with the observed system.

To quantify how well a system agrees with GJ876 we calculate a χ^2 statistic for each simulation, which we define as,

$$\chi^2 = \frac{1}{6} \sum_{i=1}^6 \left(\frac{y_i - y_{\text{obs},i}}{\sigma_{\text{obs},i}} \right)^2, \quad (5)$$

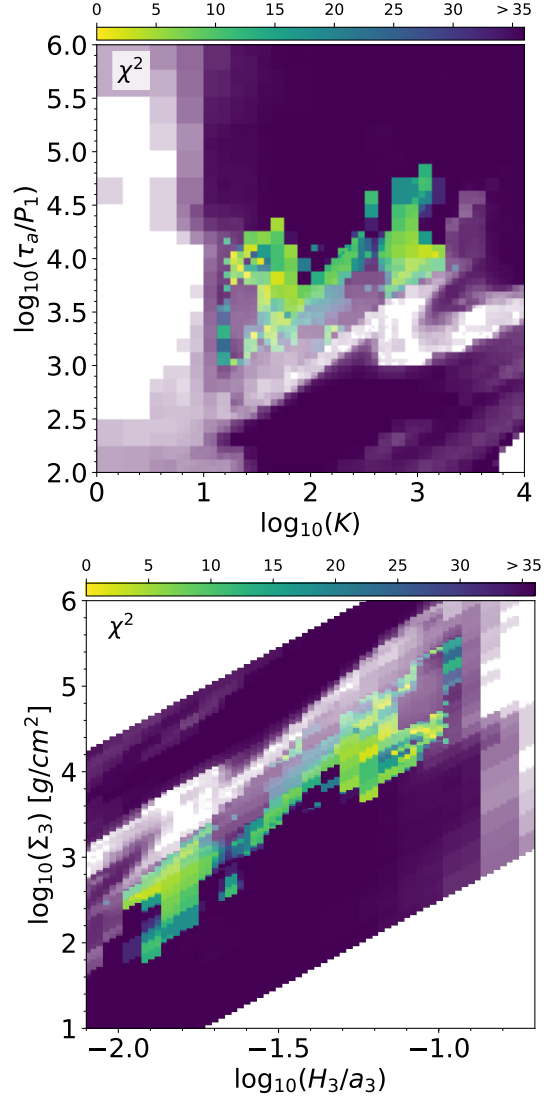


Figure 7. The χ^2 statistic defined in Equation (5). The top panel shows χ^2 as a function of K and τ_a . The bottom panel shows χ^2 as a function of disk thickness, H/a , and disk surface density, Σ at the location of the outer planet. To convert from τ_a and K to Σ and H/a we use Equations (1) and (2).

and where y_{obs} and σ_{obs} are the observed values and uncertainties of $\Phi_{1,2}$, $\Phi_{2,3}$, Φ_L , e_1 , e_2 , and e_3 . For a given (K, τ_a) pair we show the minimum χ^2 across all $\tau_{e,1}$ values in the top panel of Figure 7.

This combined statistic attains its minimum in the region of parameter space near $K \simeq 30 - 3,000$ and $\tau_a \simeq 10^3 - 10^4 P_1$. In particular, there are two regions of best fit: one around $K \simeq 30$ and $\tau_a \simeq 3 \times 10^3 - 10^4 P_1$ and another around $K \simeq 300 - 1,000$ and $\tau_a \simeq 10^4 P_1$. The region at larger K and longer τ_a corresponds to systems with weak eccentricity damping on the inner

planets (large $\tau_{e,1}$), while the region at lower K and shorter τ_a corresponds to systems with short $\tau_{e,1}$.

For simplicity we use equal weighting for the six parameters when computing χ^2 in Equation (5). If the resonant angles are given more weight in the sum, the χ^2 values generally come down since the relative uncertainties in the angles are larger, but the overall best-fit region does not change. This is clear from the top row of Figure 3 which shows that the region enclosed by the 3σ contours is the same for the three resonant angles and coincides with the overall low χ^2 region in the top panel of Figure 7. Similarly, if we give more weight to the eccentricities, the minimum χ^2 region as shown in Figure 7 experiences little change.

In the bottom panel of Figure 7 we use Equations (1) and (2) to derive a constraint on the surface density of gas and disk thickness near the outer Laplace planet. Again, there are two regions of parameter space where the simulations match the observed system particularly well. One has low surface density and thickness with $\Sigma \simeq \text{few} \times 10^2 \text{ g/cm}^2$ and $H/a \simeq 0.01 - 0.02$, and the other has a higher surface density and thickness with $\Sigma \simeq \text{few} \times 10^3 - 10^5 \text{ g/cm}^2$ and $H/a \simeq \text{few} \times 10^{-2}$. This latter region typically requires stronger eccentricity damping of the inner planets in order to drive the system into the observed configuration. In other words, if we did not damp the inner planets in addition to the outermost planet, we would infer a very thin, low surface density disk near GJ876-e at the formation time of the Laplace resonance.

As previously mentioned, these estimates depend on the overall normalizations connecting the disk properties to the semi-major axis and eccentricity damping timescales, and are best determined by hydrodynamical models (Goldreich & Tremaine 1980, 1981; Artymowicz 1993a,b; Lee & Peale 2002; Tanaka et al. 2002; Kley & Nelson 2012). Nevertheless, it is encouraging that we obtain reasonable numbers (cf. Andrews & Williams 2005) for the inner regions of GJ876’s protoplanetary disk given our simplified migration model.

3.4. Chaos

Dynamical fits to GJ876 strongly suggest that the system is chaotic with a Lyapunov timescale between tens to thousands of years (Batygin et al. 2015; Nelson et al. 2016; Martí et al. 2016; Millholland et al. 2018). The Lyapunov timescale, τ_{lyap} , characterizes the time it takes for nearly identical initial conditions to diverge, and hence is one measure of chaos (e.g. Murray & Dermott 1999). During the non-damping stage for systems deemed in the Laplace resonance, we track τ_{lyap} by integrating the variational equations and monitoring the

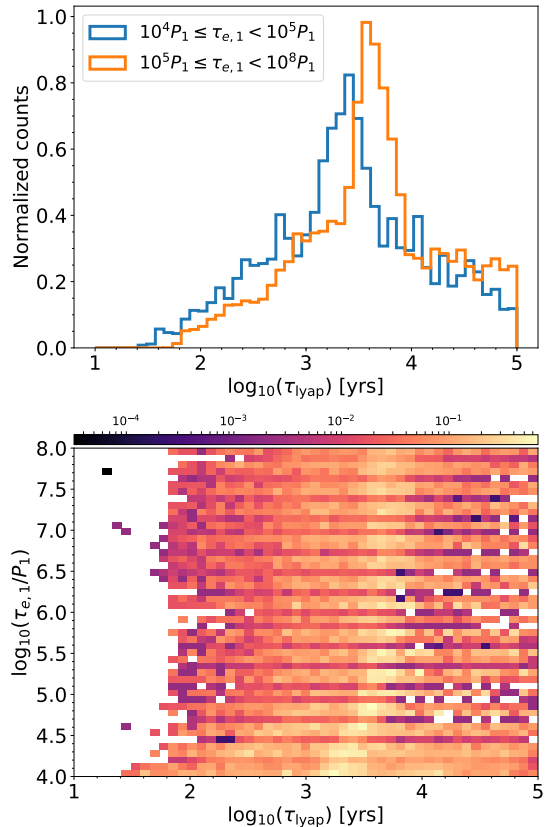


Figure 8. *Top:* Normalized histogram of τ_{lyap} for simulations with $10^4 \leq \tau_{e,1} < 10^5 P_1$ (blue line) and $10^5 \leq \tau_{e,1} < 10^8 P_1$. Because of our non-uniform grid, each simulation is given a weight of $8^{8-\ell}$, where ℓ is the level of refinement for that simulation. *Bottom:* A 2D histogram showing the dependence of τ_{lyap} on the inner planets’ eccentricity damping rate. The color of a pixel centered on a given $(\tau_{\text{lyap}}, \tau_{e,1})$ shows the total number of times across all (K, τ_a) pairs that the Lyapunov time was that value. The counts are normalized to the total number.

temporal evolution of the MEGNO number (for a description of the algorithms used see e.g.; Cincotta et al. 2003; Rein & Tamayo 2016).

The bottom right plot of Figure 3 shows the 2D distribution of τ_{lyap} for our standard set of simulations. In the resonant region, we typically find $\tau_{\text{lyap}} \gtrsim 10^3$ years, with shorter timescales on the fringes of the region.

In Figure 8 we show how the Lyapunov time varies with $\tau_{e,1}$. In the top panel, we show the distribution of τ_{lyap} for all of our simulations. Recall that we only track the chaos indicators in our simulations if they exit the damping stage with $\langle \Phi_L \rangle \leq 100^\circ$. To get a sense of the dependence on $\tau_{e,1}$, we split the distribution into systems with strong ($\tau_{e,1} < 10^5 P_1$) and weak ($\tau_{e,1} \geq 10^5 P_1$) eccentricity damping on the inner planets. The distributions are mostly similar with peaks around a few thousand years, but systems with shorter $\tau_{e,1}$ have a higher

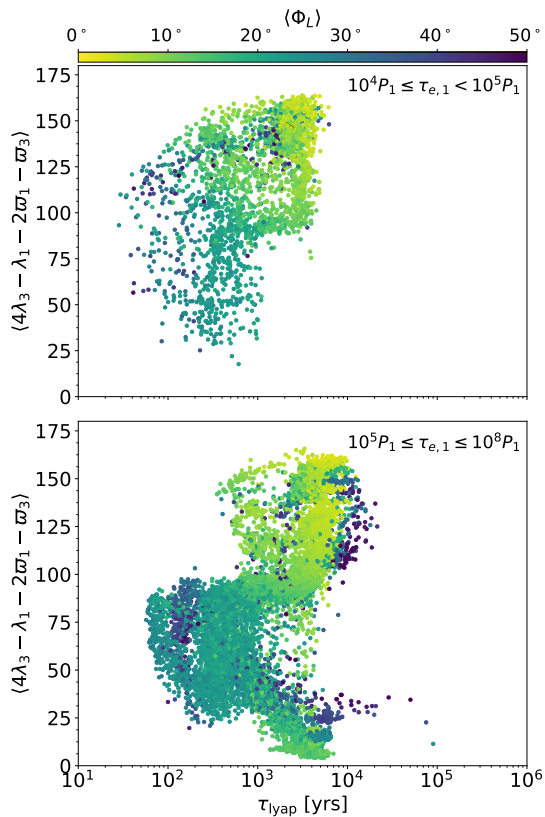


Figure 9. Correlations of the libration amplitudes for the 4:1 resonant angle, $4\lambda_3 - \lambda_1 - 2\varpi_1 - \varpi_3$, with τ_{lyap} , for two ranges of $\tau_{e,1}$. The top panel is for stronger eccentricity damping of the inner planet ($\tau_{e,1} < 10^5 P_1$), while the bottom panel is for weaker eccentricity damping ($\tau_{e,1} \geq 10^5 P_1$). Only simulations with $\langle \Phi_L \rangle \leq 50^\circ$ are shown and the color of each point corresponds to the value of $\langle \Phi_L \rangle$. Unlike for the Laplace angle, the libration amplitude here corresponds to the standard deviation (as opposed to the RMS).

chance of having $\tau_{\text{lyap}} < 10^3$ years. We explore this further in the bottom panel of Figure 8, where we show the 2D distribution of τ_{lyap} and $\tau_{e,1}$. For a given value of $\tau_{e,1}$ we compute the histogram of τ_{lyap} across all values of K and τ_a . The color of each pixel in Figure 8 shows the normalized, total number of times that particular value of τ_{lyap} occurred. Again, the peak of the distribution for all $\tau_{e,1}$ occurs around Lyapunov times of a few thousand years. At the strongest damping rates, the distribution flattens out with more occurrences of $\tau_{\text{lyap}} < 10^3$ years and $\tau_{\text{lyap}} > 10^4$ years.

3.4.1. The double apsidal corotation resonance

A longer τ_{lyap} is consistent with [Batygin et al. \(2015\)](#), who found that in addition to the decades long τ_{lyap} , there was also a region of phase space where $\tau_{\text{lyap}} \gtrsim 10^3$ years. Moreover, [Millholland et al. \(2018\)](#) associate this with a low energy, double apsidal corotation resonance

where the angles $\varpi_3 - \varpi_2$, $\varpi_2 - \varpi_1$, $2\lambda_3 - \lambda_2 - \varpi_3$, and $4\lambda_3 - \lambda_1 - 2\varpi_1 - \varpi_3$ all librate. Figure 9 shows the correlation of one of these angles, $4\lambda_3 - \lambda_1 - 2\varpi_1 - \varpi_3$, with τ_{lyap} and $\tau_{e,1}$ for simulations with $\langle \Phi_L \rangle < 50^\circ$ ⁶. This angle is associated with the 4:1 MMR between the innermost and outermost planets of the resonant chain. The top panel shows the distribution for $\tau_{e,1} < 10^5 P_1$, while the bottom panel shows the distribution for $\tau_{e,1} \geq 10^5 P_1$. Systems with $\tau_{\text{lyap}} \gtrsim 10^3$ years can either have these angles librate with small amplitude or circulate and have $\langle \Phi_L \rangle \lesssim 10^\circ$, while systems with $\tau_{\text{lyap}} \lesssim 10^3$ years have predominantly larger libration amplitudes and $\langle \Phi_L \rangle \gtrsim 10^\circ$. This large libration amplitude suggests that the angles are switching between libration and circulation as pointed out in [Millholland et al. \(2018\)](#).

Moreover, for the shortest $\tau_{e,1}$ values, we do not find any simulations where these angles have low librations amplitudes. This suggests that if the true system lies in the region of parameter space where the angles associated with the double apsidal corotation resonance librate with small amplitude, then there was little or no eccentricity damping of the inner planets at the time of the Laplace resonance formation.

4. DISCUSSION

4.1. Alternative initial conditions

Given that the majority of our simulations sit in the longer Lyapunov timescale part of phase space, we wish to now examine possible alternatives to our standard setup described in §2.2 which could potentially increase the number of initial conditions leading to $\tau_{\text{lyap}} \lesssim 10^3$ years. In Figure 10 we summarize the results of relaxing three of our initial assumptions: the timescale of the damping removal, coplanarity, and neglecting the fourth planet of the system, GJ876-d.

Abrupt damping removal—In our standard set of simulations, we slowly removed the damping forces on the outer planet over one damping timescale. We ran an additional set of simulations where we instead abruptly turned off all damping forces. The distribution of τ_{lyap} as shown in the top panel of Figure 10 is relatively insensitive to how smoothly the damping forces are removed. The only significant change is slightly more systems to the left of the main peak at $\tau_{\text{lyap}} \simeq 3000$ years.

Mutual inclinations—Another major simplification of our study is in assuming that the Laplace planets are copla-

⁶ The other angles associated with the double apsidal corotation resonance show the same correlation with τ_{lyap} and $\tau_{e,1}$.

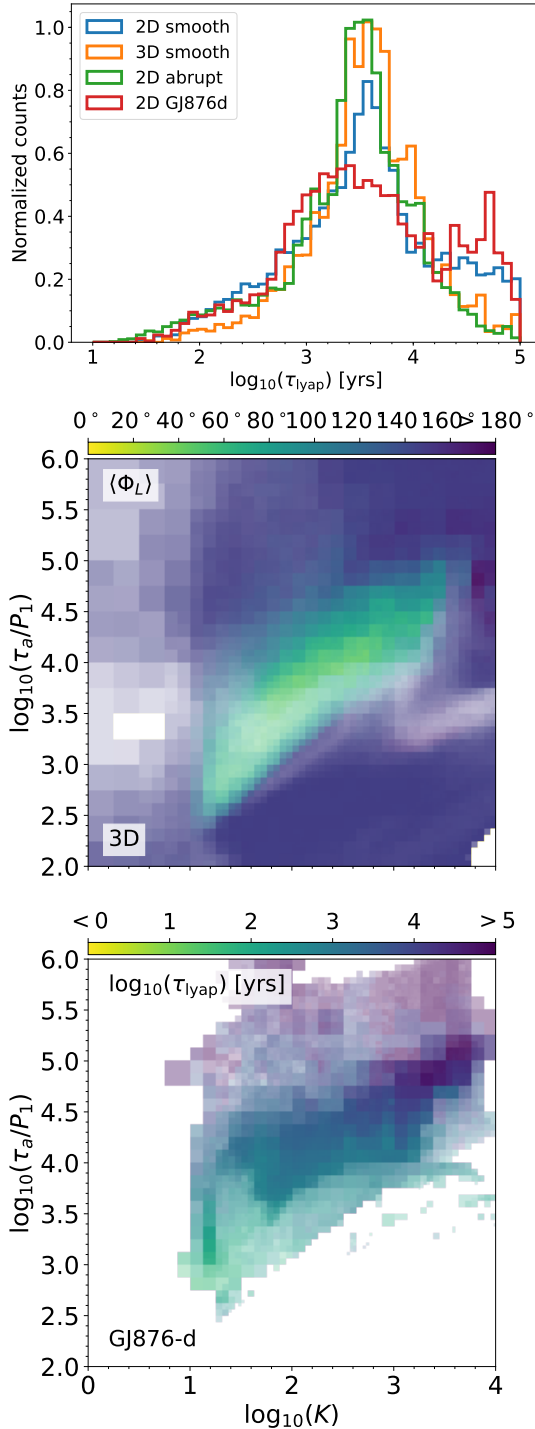


Figure 10. Results from variations on our initial setup. *Top:* The distribution of τ_{lyap} for the different setups described in §4.1. *Middle:* The $\tau_{e,1}$ integrated $\langle \Phi_L \rangle$ for the 3D setup. *Bottom:* The $\tau_{e,1}$ integrated τ_{lyap} for the setup which includes GJ876-d.

nar with each other. This is a relatively robust assumption, however, since the observed Laplace planets are nearly coplanar (Nelson et al. 2016). Nevertheless, we ran an additional set of simulations where we gave each planet a random initial inclination of up to 20° . The distribution of τ_{lyap} is relatively unaffected by allowing the planets to be mutually inclined. The middle panel of Figure 10 shows that allowing the planets to have non-zero inclinations narrows the Laplace resonance parameter space and increases the instability fractions.

GJ876-d—The two-day inner planet, GJ876-d ($M_d \simeq 7M_\oplus$, $P_d = 1.94d$, $e_d \simeq 0.11$ ⁷), has so far been neglected in the resonance capture and subsequent evolution of our models (Nelson et al. 2016). While this is likely a good assumption for the process of resonance capture, it is less so when studying the overall system parameters (such as instability and chaos) during the long term evolution of the entire system. To this end, we ran our standard set of simulations again, but after removing the damping forces we additionally included GJ876-d at its observed period and eccentricity. When GJ876-d is included, we also include the precessional effects of GR via REBOUNDX (Nobili & Roxburgh 1986). Including GJ876-d does not noticeably affect the distribution for $\tau_{\text{lyap}} < 10^3$ years. Surprisingly, however, it does increase the frequency of systems with $\tau_{\text{lyap}} > 10^4$ years.

Additionally, other effects not present in our simplified smooth migration models, such as the stochastic forcing used in Batygin et al. (2015), or the presence of an eccentric disk during the damping phase (e.g. Kley et al. 2005), may shorten or significantly affect the chaotic timescale of the system.

5. CONCLUSIONS AND FUTURE WORK

Since the majority of parameter space where GJ876 is in resonance has $\langle \Phi_L \rangle \lesssim 10^\circ$ and $\tau_{\text{lyap}} \gtrsim 10^3$ years, it is somewhat surprising that the observed system has such large libration amplitude and short Lyapunov time. Further observations of the system will yield better constraints on these two characteristics as well as on the eccentricities of the planets (Millholland et al. 2018). In particular, the eccentricity of GJ876-c provides the strongest constraint on the appropriate damping timescales driving the system into resonance.

In addition to further observations, more detailed, hydrodynamical simulations of the three Laplace planets in GJ876 are required to determine whether or not the formation scenario we have presented here is truly vi-

⁷ We use the larger eccentricity from Nelson et al. (2016) as opposed to the smaller eccentricity from Millholland et al. (2018).

able. In particular, such simulations can help explain how an eccentric disk (Kley et al. 2005), the presence of an inner disk (Crida et al. 2008), how the disk disperses (Kley et al. 2005), the level of disk viscosity (e.g. Fung & Chiang 2017), and other effects determine the migration rates, final eccentricities, resonance angles, and Lyapunov timescale of GJ876. Hydrodynamical simulations will also improve upon the connection between damping timescales and disk properties (e.g. Equations (1) and (2)).

On this topic, Cimerman et al. (2018) have recently simulated the construction of the Laplace resonance in GJ876 for several different disk thicknesses, masses, and viscosities using hydrodynamical simulations of two-dimensional locally isothermal disks. Compared to our smooth migration model, the migration rate of GJ876-e in their simulations can vary wildly with time as the presence of an eccentric disk outside of GJ876-c,b induces large variations in the torque felt by the outer planet. In many of their cases this prevents the system from forming the 4:2:1 MMR as GJ876-e is caught at larger period ratios with GJ876-b. In order to form the Laplace resonance, they offer two main avenues. The first is for GJ876-e to open a partial gap in the disk, allowing it to gradually remove the disk eccentricity induced by GJ876-b,c and migrate into the 2:1 resonance with GJ876-b. This scenario requires the disk thickness and viscosity to be low enough for GJ876-e to open a (partial) gap. The second is for the resonance capture to take place later in the systems lifetime when the disk surface density is lower. Further simulations covering a wider range of thicknesses and disk masses would facilitate a more robust comparison to our results (e.g. to Figure 7).

A natural extension of our AMR method is to the study of other resonant chain systems. While GJ876

is unique in its diversity of masses, systems discovered by *Kepler* typically have roughly equal mass planets orbiting their host star in a compact configuration. Our method can be readily applied to systems containing resonant chains of Earth mass, or Super-Earth mass planets, and can put meaningful constraints on the local disk properties present when the planets captured into resonance (see also e.g. Delisle et al. 2015). Examples of such systems include Kepler-60, Kepler-223, Trappist 1, and others (Mills et al. 2016; Goździewski et al. 2016; Luger et al. 2017). In particular, chains of non-gap opening planets may undergo Type I migration, and if they have measured masses, the parameter space to explore consists only of the density and temperature profile of the disk. This low-dimensional parameter space allows for our efficient AMR scheme to fully explore the relevant parameter space.

The mesh refinement code used is available at <http://github.com/adamdempsey90/NDTAMR>. We would like to thank the referee for a thorough and insightful report which greatly improved the manuscript. We would also like to thank Sam Hadden, Yoram Lithwick, Diego Muñoz, Matt Payne, Hanno Rein, and Dan Tamayo for useful discussions, as well as Sarah Millholland and Greg Laughlin for sharing an early version of their paper with us. This research was supported in part through the computational resources and staff contributions provided for the Quest high performance computing facility at Northwestern University which is jointly supported by the Office of the Provost, the Office for Research, and Northwestern University Information Technology. B.E.N. acknowledges support from the Data Science Initiative at Northwestern University.

REFERENCES

- Andrews, S. M., & Williams, J. P. 2005, *ApJ*, 631, 1134
- Artymowicz, P. 1993a, *ApJ*, 419, 155
- . 1993b, *ApJ*, 419, 166
- Bai, X.-N., & Stone, J. M. 2013, *ApJ*, 769, 76
- Balbus, S. A., & Hawley, J. F. 1991, *ApJ*, 376, 214
- Batygin, K., Deck, K. M., & Holman, M. J. 2015, *AJ*, 149, 167
- Berger, M. J., & Colella, P. 1989, *JCP*, 82, 64
- Cimerman, N. P., Kley, W., & Kuiper, R. 2018, [arXiv:1808.04223](https://arxiv.org/abs/1808.04223)
- Cincotta, P. M., Giordano, C. M., & Simó, C. 2003, *Phys. D: Nonlinear Phenomena*, 182, 151
- Correia, A. C. M., Couetdic, J., Laskar, J., et al. 2010, *A&A*, 511, A21
- Crida, A., Sándor, Z., & Kley, W. 2008, *A&A*, 483, 325
- Deck, K. M., & Batygin, K. 2015, *ApJ*, 810, 119
- Delisle, J. B., Correia, A. C. M., & Laskar, J. 2015, *A&A*, 579, A128
- Dürmann, C., & Kley, W. 2015, *A&A*, 574, A52
- Fryxell, B., Olson, K., Ricker, P., et al. 2000, *ApJS*, 131, 273
- Fung, J., & Chiang, E. 2017, *ApJ*, 839, 100
- Goldreich, P., & Sari, R. 2003, *ApJ*, 585, 1024
- Goldreich, P., & Schlichting, H. E. 2014, *AJ*, 147, 32
- Goldreich, P., & Tremaine, S. 1980, *ApJ*, 241, 425

- . 1981, *ApJ*, 243, 1062
- Goździewski, K., Migaszewski, C., Panichi, F., & Szuszkiewicz, E. 2016, *MNRAS: Letters*, 455, L104
- Kley, W., Lee, M. H., Murray, N., & Peale, S. J. 2005, *A&A*, 437, 727
- Kley, W., & Nelson, R. P. 2012, *ARA&A*, 50, 211
- Lee, M. H., & Peale, S. J. 2002, *ApJ*, 567, 596
- Lesur, G., Kunz, M. W., & Fromang, S. 2014, *A&A*, 566, A56
- Löhner, R. 1987, *Computer Methods in Applied Mechanics and Engineering*, 61, 323
- Luger, R., Sestovic, M., Kruse, E., et al. 2017, *Nature Astronomy*, 1, 0129
- Marcy, G. W., Butler, R. P., Vogt, S. S., Fischer, D., & Lissauer, J. J. 1998, *ApJ*, 505, L147
- Martí, J. G., Cincotta, P. M., & Beaugé, C. 2016, *MNRAS*, 460, 1094
- Millholland, S., Laughlin, G., Teske, J., et al. 2018, *The Astronomical Journal*, 155, 106
- Mills, S. M., Fabrycky, D. C., Migaszewski, C., et al. 2016, *Nature*, 533, 509
- Murray, C. D., & Dermott, S. F. 1999, *Solar System Dynamics*. Cambridge Univ. Press, Cambridge.
- Nelson, B. E., Robertson, P. M., Payne, M. J., et al. 2016, *MNRAS*, 455, 2484
- Nobili, A., & Roxburgh, I. W. 1986, in *Relativity in Celestial Mechanics and Astrometry. High Precision Dynamical Theories and Observational Verifications*, ed. J. Kovalevsky & V. A. Brumberg, 105–110
- Papaloizou, J. C. B., & Larwood, J. D. 2000, *MNRAS*, 315, 823
- Rein, H., & Liu, S. F. 2012, *A&A*, 537, A128
- Rein, H., Papaloizou, J. C. B., & Kley, W. 2010, *A&A*, 510, A4
- Rein, H., & Spiegel, D. S. 2015, *MNRAS*, 446, 1424
- Rein, H., & Tamayo, D. 2015, *MNRAS*, 452, 376
- . 2016, *MNRAS*, 459, 2275
- Rivera, E. J., Laughlin, G., Butler, R. P., et al. 2010, *ApJ*, 719, 890
- Simon, J. B., Lesur, G., Kunz, M. W., & Armitage, P. J. 2015, *MNRAS*, 454, 1117
- Snellgrove, M. D., Papaloizou, J. C. B., & Nelson, R. P. 2001, *A&A*, 374, 1092
- Tamayo, D., Rein, H., Petrovich, C., & Murray, N. 2017, *ApJL*, 840, L19
- Tanaka, H., Takeuchi, T., & Ward, W. R. 2002, *ApJ*, 565, 1257
- Tanaka, H., & Ward, W. R. 2004, *ApJ*, 602, 388
- Trifonov, T., Kürster, M., Zechmeister, M., et al. 2018, *Astronomy and Astrophysics*, 609, A117
- van Leeuwen, F. 2007, *Astrophysics and Space Science Library*, Vol. 350, *Hipparcos, the New Reduction of the Raw Data*, ed. F. van Leeuwen. Springer Netherlands, Dordrecht
- von Braun, K., Boyajian, T. S., van Belle, G. T., et al. 2014, *MNRAS*, 438, 2413
- Ward, W. R. 1997, *Icarus*, 126, 261